ARTICLE IN PRESS

Journal of the European Ceramic Society xxx (xxxx) xxx

Contents lists available at ScienceDirect

Journal of the European Ceramic Society

journal homepage: www.elsevier.com/locate/jeurceramsoc

Solution precursor thermal spraying of gadolinium zirconate for thermal barrier coating

K. Leng, A. Rincon Romero, F. Venturi, I. Ahmed, T. Hussain *

Coatings and Surface Engineering, Advanced Materials Research Group, Faculty of Engineering, University of Nottingham, NG7 2RD, United Kingdom

ARTICLE INFO

Keywords:
Gadolinium zirconate
Yttria stabilised zirconia
TBC
Solution precursor
Suspension HVOF

ABSTRACT

Gadolinium zirconate (GZ) is an attractive material for thermal barrier coatings (TBCs). However, a single layer GZ coating has poor thermal cycling life compared to Yttria Stabilized Zirconia (YSZ). In this study, Solution Precursor High Velocity Oxy-Fuel (SP-HVOF) thermal spray was used to produce a double layer GZ/YSZ TBC and compared the thermal cycling performance with the single layer YSZ TBC. The temperature behaviour of the solution precursor GZ was studied, and single splat tests were carried out to obtain an optimised spray parameter. In thermal cycling tests, the single-layer YSZ reached 20 % failure at 85 ± 5 cycles, whereas the double-layer GZ/YSZ was at 70 ± 15 cycles. The single-layer failed at the topcoat/TGO interface, whereas the double-layer failed at GZ/YSZ interface and topcoat/TGO interface. Moreover, Gd diffusion occurred near the GZ/YSZ interface, resulting in porosities in the GZ layer.

1. Introduction

Thermal barrier coatings (TBCs) are widely used in several industrial applications (i.e., automotive, aerospace, power generation) to protect critical components from harsh thermomechanical conditions. The primary purpose of TBCs is to create a thermal gradient across the surface of components, thereby extending the life cycle and durability of components. A significant reduction in the surface temperature of these components, generally in the range between 100 °C and 300 °C, could be achieved with these coatings [1,2]; however, this is dependent on the coating's thickness which is defined by its deposition techniques (i.e., thermal spray, electron beam physical vapour deposition) as well as the functionality (i.e., rotating/static) of the component.

Zirconia based ceramics, typically 7–8 wt.% Yttria Stabilized Zirconia (YSZ), is widely used as the ceramic topcoat for turbine blades due to its low thermal conductivity and a high coefficient of thermal expansion. However, YSZ topcoat is limited to provide thermal insulation at a maximum temperature of 1200 °C [3–7]. Beyond 1200 °C, YSZ will transform from the metastable tetragonal phase (t') into tetragonal (t) and cubic phases (c). Subsequently, the tetragonal phase will further transform into monoclinic phase (m) upon cooling. As such, cracks are introduced in the system as the phase transformation of YSZ is associated with 3–5 % of volume change in the microstructure, leading to coating failure [5,8]. Moreover, the operating temperature above 1200 °C has introduced another issue for the current TBC (i.e., YSZ), namely CMAS (Calcium-Magnesium-Alumina-Silicate) attack. Although the composition of CMAS varies, the majority of CMAS has a melting temperature in the range of 1200 °C.

The limitation of YSZ has initiated the findings of new ceramic material to overcome the problems associated with YSZ. The new ceramic material has to operate above 1200 °C without sacrificing other properties such as phase stability at high temperature, low thermal conductivities, and sintering resistance at high temperatures [4]. In many recent studies, researchers had narrowed down the scope to rare-earth (RE) zirconates based pyrochlores. Among all RE zirconates, gadolinium zirconate (GZ) gained special attention because other rare-earth zirconates such as lanthanum zirconate (LZ) have the tendency to lose their stoichiometry during the deposition process [9,10]. In comparison with YSZ, GZ offers promising properties like lower thermal conductivities, a better CMAS resistance, a better sintering resistance at elevated temperatures, and good phase stabilities beyond 1500 °C. Moreover, GZ can resist CMAS attack by reacting with CMAS to form a metastable apatite phase (i.e., $Ca_2Gd_8(SiO_4)_6O_2$) to stop the infiltration of CMAS [8,11–16]. Despite these advantageous features, GZ has a relatively low coefficient of thermal expansion (CTE), resulting in a much lower fracture toughness and also a high tendency to react with thermally grown oxide (TGO) layer. For instance, GZ shows poor thermal cycling performances and a higher tendency to initiate crack

---

* Corresponding author.
E-mail address: Tanvir.Hussain@nottingham.ac.uk (T. Hussain).

https://doi.org/10.1016/j.jeurceramsoc.2021.11.050
Received 20 August 2021; Received in revised form 11 November 2021; Accepted 23 November 2021

Please cite this article as: K. Leng, *Journal of the European Ceramic Society*, https://doi.org/10.1016/j.jeurceramsoc.2021.11.050

propagations even at a low stress level. Additionally, GZ has the tendency to react with alumina (TGO) to form $GdAlO_3$, resulting in an extremely low number of thermal cyclic life compared to the single-layer YSZ [17,18]. To account the drawbacks of GZ, a double-layer approach has been proposed, having GZ as the topcoat ceramic followed by the YSZ as the second layer [14,19,28,20–27].

Air Plasma Spray (APS) is the most widely available deposition technique by the industry; however, this technique is difficult to produce the columnar microstructure achievable by the more expensive Electron Beam Physical Vapor Deposition (EB-PVD) deposition process.The commonly known columnar structure in EB-PVD offered strain-tolerant capabilities to the coating structure, resulting in an excellent thermal cycling performance [29]. Deposition of nanoparticles with thermal spray required suspension or solution precursor as a carrier medium. Suspension thermal spray can produce significantly improved coating microstructure due to their smaller particle size and interaction of these particles with the flame. Studies demonstrated that both the Suspension High Velocity Oxy-Fuel (S-HVOF) and suspension plasma spray (SPS) techniques have the ability to produce dense vertical cracks to alleviate thermal stresses during thermal cycling tests [30–32]. On the other hand, the solution precursor thermal spray eliminates the need to suspend particles in a medium, either in water or ethanol, by mixing solutes (i.e., salts) into a solvent (i.e., water).

In previous studies, APS sprayed double-layer GZ/YSZ by Bakan et al. [17,25,33] demonstrated that the thermal cycling performance of GZ was sensitive to the coating porosity and GZ stoichiometry. The dense coating possessed a lower lifetime under the burner rig test and spallation at the GZ/YSZ interface was observed while the porous coating structure (15 % porosity) spalled at the TBC/bond coat interface. Mahade et al. [27,34] reported that the suspension plasma sprayed (SPS) double-layered TBCs' durability was affected by the YSZ thickness, in which its life cycle decreased with YSZ thickness. The study also reported that the failure mode of the double-layered TBCs varied under different thermal cyclic test conditions, isothermal and thermal gradient conditions. In an isothermal condition, the SPS sprayed double-layered GZ/YSZ failed only at the TGO/bond coat interface whereas failures at both TGO/bond coat interface and GZ/YSZ interface were observed for thermal gradient conditions. On the other hand, Jiang et al. [14] is the only study that produced the double-layered GZ/YSZ with solution precursor plasma spray (SPPS). The SPPS sprayed double-layered GZ/YSZ TBC was reported to show a better thermal cycling lifetime compared to both APS and SPPS sprayed single-layer YSZ TBCs. Despite the low fracture toughness in GZ, it did not show notable deterioration in thermal cycling performance. Likewise, the SPPS sprayed double-layered GZ/YSZ TBC failed at the TGO/bond coat interface under an isothermal thermal cycling condition. The SPPS microstructure benefited from vertical cracks (VCs) to alleviate stresses generated in the coatings, showed an improved version to that of traditional APS coatings [14,35,36].

Improved durability in all plasma-sprayed double-layer TBCs was observed; however, the increasing popularity of S-HVOF (suspension HVOF) or SP-HVOF (solution precursor HVOF) warrants an investigation in double-layered TBC deposition. In this study, a single-layer YSZ and a double-layer GZ/YSZ were deposited by HVOF thermal spray process (YSZ from S-HVOF and GZ from SP-HVOF) on bond coated Inconel 718 substrates. The bond coat composition chosen for this study was CoNiCrAlY which was deposited by a liquid-fuelled HVOF thermal spray [37]. The effort was spent developing the process parameters for the successful deposition of the solution precursor GZ to achieve the desired coating structure and excellent bonding at the GZ/YSZ interface. Isothermal thermal cycling tests were performed side-by-side for the single-layer YSZ and double-layer GZ/YSZ at 1135 ℃, with the single-layered S-HVOF YSZ as a baseline sample.

2. Experimental methods

2.1. Materials

Two types of feedstock materials were used in this study, (a) solution precursor Gadolinium Zirconate (GZ) and (b) suspension Yttria-stabilized Zirconia (YSZ). GZ solution precursor were made by dissolving gadolinium nitrate hexahydrate (Fisher Scientific, Loughborough, UK) into distilled (DI) water to 2 mol/L. The solution was then added to a 2 mol/L zirconium acetate (22 wt. % ZrO_2 in diluted acid, Sigma Aldrich, Dorset, UK) aqueous solution and both solutions were mixed in stoichiometric proportion to reach the desired GZ phase. The final solution yielded 10 % of GZ.

The 8 wt.% yttria stabilised zirconia (YSZ) suspension in ethanol was provided by Treibacher Industrie AG (Althofen, Austria); the suspension had a solid loading of 25 wt.% and a particle size distribution of D_{50} = 0.50 μm, according to the supplier.

2.2. Swipe test

AISI SS304 stainless steel substrates (60 × 25 × 2 mm^3) with a nominal composition of Fe-19.0Cr-9.3Ni-0.05C (in wt.%) were used to collect single splats of the GZ coatings. Prior to the single splat deposition, all stainless steel substrates were ground using SiC grinding papers (Essligen, Germany) and polished to 1 μm finish with diamond suspension.

The splats were deposited using a modified GTV SS-TopGun HVOF thermal spray system with an injector diameter of 0.3 mm directed towards a 22 mm long combustion chamber on the substrates. The details of the setup can be found elsewhere [30]. The gun was mounted on a 6-axis robot (ABB® IRB 2400, Warrington, UK) that provide the spraying motion, a standard raster scan pattern. The torch speed was set at 1361 mm/s, and the inter line spacing was adjusted to produce 3 equally spaced splat lines across the polished substrates. Two sets of spray parameters were used, corresponding to the variation of stand-off distance and the flow rate of feedstocks. The stand-off distances were chosen: 75 mm, 85 mm and 95 mm while the flow rate of feedstocks remained at 50 mL/min. Specimens generated using the above stand-off distance were designated as SOD75, SOD85 and SOD95, respectively. The flow rate of feedstocks was varied at three different levels of 30 mL/min, 40 mL/min and 50 mL/min while the stand-off distance remained at 85 mm. Specimens generated using the above flow rate were designated as FLR30, FLR40, and FLR50, respectively.

2.3. Coating deposition

Disc-shaped Inconel 718 substrates of 12.7 × 3 mm dimension and nominal composition of Ni-19.0Cr-3.0Mo-5.1Nb-0.5Al-0.9Ti-18.5Fe-0.04C (in wt.%) were used for coating deposition. All Inconel 718 substrates were grit blasted with a blast cleaner from Guyson (Dudley, UK) with fine F100 brown alumina (0.125 – 0.149 mm) particles at 6 bars. Following grit blasting, the substrates were cleaned in Industrial Methylated Spirit (IMS) using an ultrasonic bath for up to 4 min and blown dry with compressed air.

Initially, a bond coat that promotes adhesion of the sprayed ceramic topcoat and provides oxidation resistance at high temperature was deposited. All disc-shaped substrates were pre-coated with approximately 130 μm Co-based bond coat, MCrAlY (CoNiCrAlY) powder (CO-210-24, Praxair, Swindon, UK) applied by using HVOF thermal spraying with a commercial MetJet IV (Metallisation, Dudley, UK) gun. A more detailed deposition of bond coat is described by Saeidi et al. [37]. The torch scanning speed was set at 1000 mm/s. The line spacing for the bond coat was 4 mm, and line spacing for topcoat was 3.5 mm, respectively to factor in the nozzle diameter.

Two types of topcoats were produced, which comprised of the YSZ single-layer and GZ/YSZ double-layer. The thermal spray system used to deposit the coating was discussed in Section 2.2., and they were optimised to obtain a GZ/YSZ double-layer topcoat, with a thickness ratio 1:1. The spray parameters were summarised in Table 1 and Fig. 1 represents the schematic diagram of the samples developed in this study.

2.4. Characterisation of GZ solution precursor

SDT-Q600 equipment (TA Instruments, New Castle, USA) was used to analyse the thermal stability and the reactions experienced by the gadolinium zirconate solution precursor. An approximate amount of 15 mg of the solution precursor was placed in the Al_2O_3 crucible. The furnace was ramped at 10 ℃/min to 1450 ℃ in a constant supply of air at a flow rate of 100 mL/min.

The solution precursor of gadolinium zirconate (GZ) was heat-treated in a box furnace (Elite Thermal Systems Ltd.) at 600 ℃, 700 ℃, 800 ℃, 1000 ℃, 1200 ℃ and 1400 ℃ for an hour at a ramp rate of 10 ℃/min to study the phase evolution of the GZ solution precursor.

2.5. Microstructural characterisation

All samples were characterised in the as-sprayed condition and after thermal cycled tests. XRD analysis was performed using a D8 Advance DaVinci system (Bruker, Coventry, UK) with equipped with a lynx eye detector. The diffractograms were obtained with Cu-Kα radiation with a wavelength of 1.54 Å in Bragg-Brentano configuration in the range from 10°to 90°2, using a 0.02°step size and 0.15 s of counting time in each step. The phase identification was performed using the DIFFRACT.SUITE EVA software (Bruker, Coventry, UK).

The produced samples were cold mounted in epoxy using vacuum impregnation and then cross-sectioned with SiC precision cut-off wheels (MetPrep, Coventry, UK) at a relatively slow speed (0.005 mm/s) to reduce the damage to the sample during the cutting process.

All sectioned samples were sequentially ground with SiC abrasive papers (MetPrep, Coventry, UK) P240, P400, P800 and P1200, respectively. The polishing process was carried out by diamond polishing up to a surface finish of 1 μm.

JSM-6490LV (JEOL, Massachusetts, USA) scanning electron microscopy (SEM) was used for structural characterisation of the single splats and coatings, using secondary electron (SE) and back-scattered electron (BSE) modes. A spot size of 50–60 nm, a working distance of 9 mm and an acceleration voltage of 20 kV were used as the imaging parameters.

ImageJ analysis suite (NIH, USA) was used to measure the thickness of the coating. The reported data represents the average and standard error of the coating thickness using secondary electron images (x300) covering 1 cm of the coating cross-section with 5 images.

Table 1
Parameters Employed for HVOF Bond-coat and Solution Precursor HVOF Gadolinium Zirconate Topcoat.

Parameters	Bond coat (CO-210−24)	Suspension Yttria Stabilized Zirconia [30] [38],	Solution Precursor Gadolinium Zirconate
Torch	MetJet (IV) Metallisation Gun	Suspension TopGun	Suspension TopGun
Stand-off distance(mm)	356	85	85
Scan speed (mm/s)	1000	1000	1000
Scan line distance (mm)	4	3.5	3.5
N_2 carrier gas flow rate (L/min)	11.00	–	–
H_2 flow rate (L/min)	–	699.98	613.60
O_2 flow rate (L/min)	920.00	299.72	306.80
Kerosene flow rate (mL/min)	476	–	–
Nozzle length (mm)	100	22	22
Powder feed rate (g/min)	(70)	–	–
Suspension flow rate (mL/min)	–	40	40
Flame power (kW)	–	99	101
Number of passes	6	25	50

2.6. Thermal cycling durability test

Four samples of each topcoat (i.e., single-layer YSZ and double-layer GZ/YSZ) were subjected to thermal cycling tests. Prior to the thermal cycling tests, all samples were heat-treated at 1135 ℃ for 2 h at a ramp rate of 5 ℃/min to ensure that there were no residues of the precursor left in the coating. Each cycle of the thermal cyclic tests comprised of heating up to 1135 C in 10 min, dwelling for 45 min, and forced air-cooling below 100 ℃ in approximately 30 min with a programmable bottom-loading isothermal furnace (CM Furnaces Inc., Bloomfield, USA). A high definition Webcam (Logitech C930e) was used to capture the image of each sample and ImageJ software was used to evaluate the area of spallation of the thermal cycled samples. The spallation area of more than 20 % was defined as failure (Fig. 2).

3. Result

3.1. Thermal characteristics of GZ precursor

It is important to understand the thermal characteristics of the solution precursor because their high temperature behaviour is critical for deposition. Fig. 3 shows the DSC-TGA measurement of the GZ precursor used in this study. The DSC-TGA analysis performed on the solution precursor evidenced that there was a predominant endothermic reaction that happened at approximately 104 ℃, which corresponds to 83 % of weight lost, and it was caused by the evaporation of water used in the precursor. Two consecutive exothermic reactions occurred at 300 ℃ and 350 ℃, and these are associated with a 7% weight loss in the TGA curve. These two exothermic peaks indicated a combination of endothermic reaction by gadolinium nitrates and the pyrolysis of zirconium acetates present in the precursor [39–41]. At 782 ℃, an endothermic peak with no correlated weight loss that could be associated with the crystallisation of GZ was detected [42]. The weight remained unchanged from 350 ℃; this could be seen as an indication that all residue organic compounds were fully decomposed at this temperature, and the precursor was transformed to 10 % weight of GZ. The phase transformations detected by the thermogravimetric study were also followed by XRD analysis, as presented in Fig. 4. Before the crystallisation temperature of GZ phase, the sample presented an amorphous structure as revealed by the humps in the diffractogram at 600 ℃. This indicated that the crystallisation of GZ had not started. For temperatures above 800 ℃, crystalline GZ (PDF Card #00-080-0471) was detected as the only crystalline phase.

3.2. Single particle impact test of the GZ precursor

As mentioned in Section 2.2, swipe tests were carried out to study the morphology of single splat varied at two distinctive parameters: stand-off distance differentiated into three distinct distances at 75 mm, 85 mm and 95 mm, and flow rates varied at 30 mL/min, 40 mL/min and 50 mL/min. SEM characterisation for both parameters for the single splat is shown in Figs. 5 and 6, respectively. The flame power for both conditions was 101 kW to ensure enough heat was transferred to the solution precursor to melt the particles formed in-flight prior to impacting onto the substrate.

According to Sunil et. al. [43],], the modelling result on the SHVOF

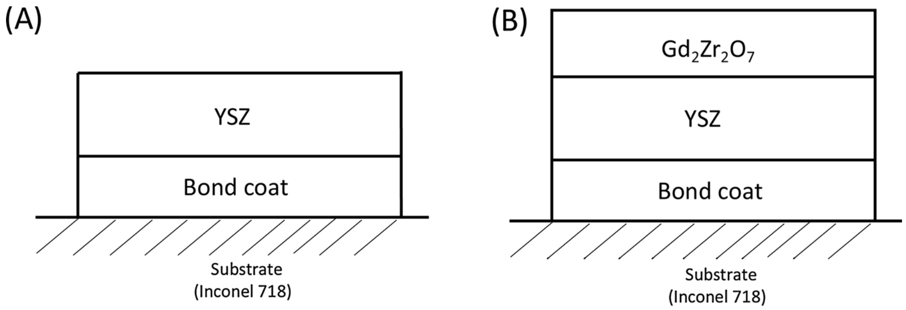

Fig. 1. (A) shows the schematic diagram of a single-layer YSZ sample, and (B) the double-layer GZ/YSZ on the substrate Inconel 718 used in this study.

Fig. 2. A programmable bottom-loading isothermal furnace with a camera recording the live time of thermal cycling samples.

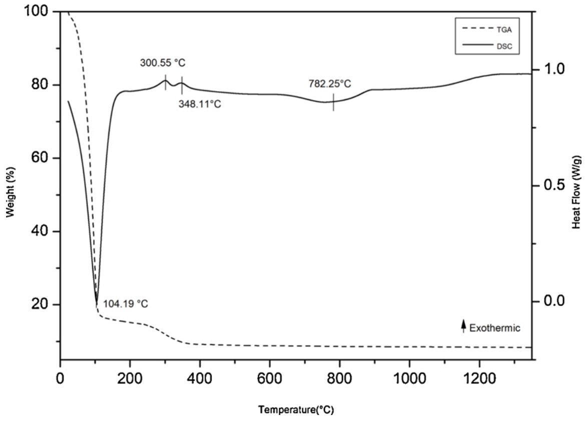

Fig. 3. Plot of DSC heat flow and TGA weight analysis of GZ solution precursor at a heating rate of 10 °C/min in a constant supply of air atmosphere.

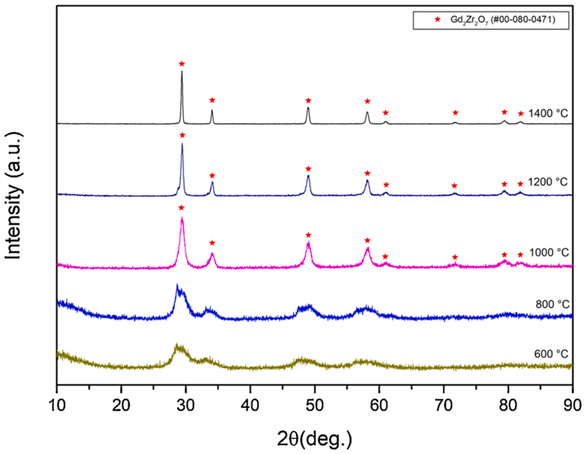

Fig. 4. XRD patterns for heat-treated GZ solution precursor powders at 600 °C, 700 °C, 800 °C, 1000 °C, 1200 °C and 1400 °C.

thermal spray was capable of achieving a maximum particle temperature of 2000 K (i.e., 1726.85 °C). Although the material used in this study was different to the material used in the modelling result, the chosen spray parameters were similar. The available heat in the combustion flame was enough to melt in-flight particles, which crystallised at 782 °C (Fig. 3). As appreciated from Fig. 5a (higher magnification image at Fig. 5d), the SOD75 sample is mostly dominated by a mixture of unmolten and partially molten particles with a small number of re-solidified agglomerates. Meanwhile, the SOD85 sample (i.e., Fig. 5b, higher magnification at Fig. 5e) presents a high degree of molten splats (in the form of splash like splats) with a small number of partially molten particles [44]. In the case of SOD95 sample (i.e., Fig. 5c, higher magnification at Fig. 5f), the sample showed a lower amount of molten splats, and the size of the deposited splats was reduced, which could have contributed to the reduced deposition efficiency at a longer stand-off distance.

Fig. 6 shows SEM micrographs of single splats collected at three different flow rates mentioned above. ImageJ analysis software was used to measure the area coverage of splats for each sample, using the “threshold” option to differentiate the substrate (dark grey region) and the splats or the individual solid particles (white spots or spheres). After differentiating the splats, the area coverage of the substrate was then measured. The reported data in Table 2 represents the average and standard error of splats coverage on the substrate with 3 measurements.

The deposition efficiency seems to be the highest for the flow rate at

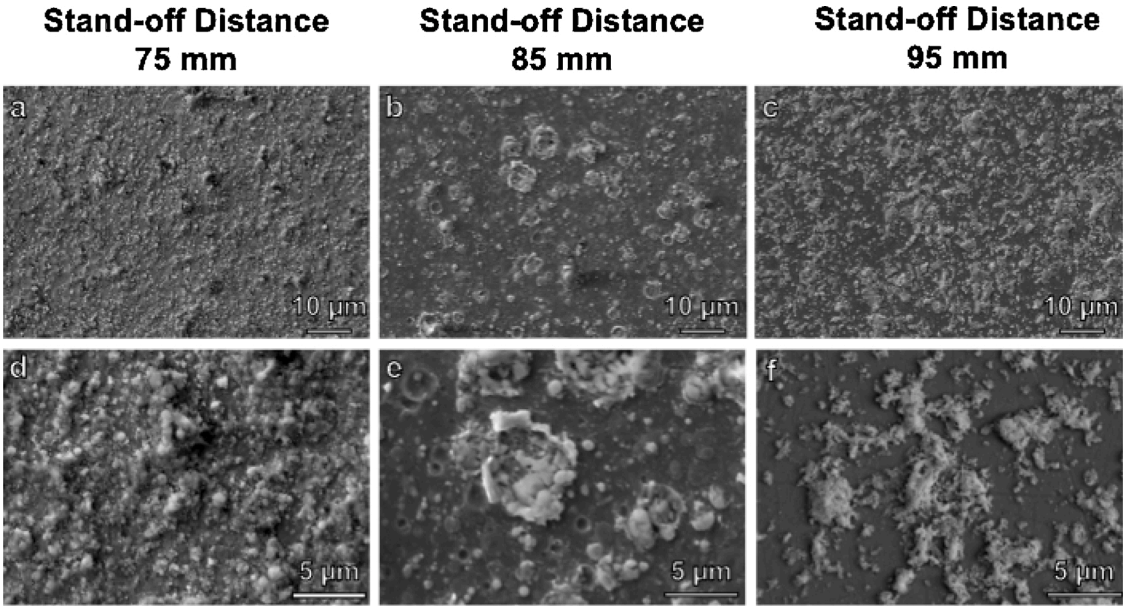

Fig. 5. Secondary Electron (SE)-SEM images for swipe test at three different stand-off distances (a) 75 mm – SOD75, (b) 85 mm – SOD85 and (c) 95 mm – SOD95, respectively, being images d to f at high magnification. All images were taken at 15 kV.

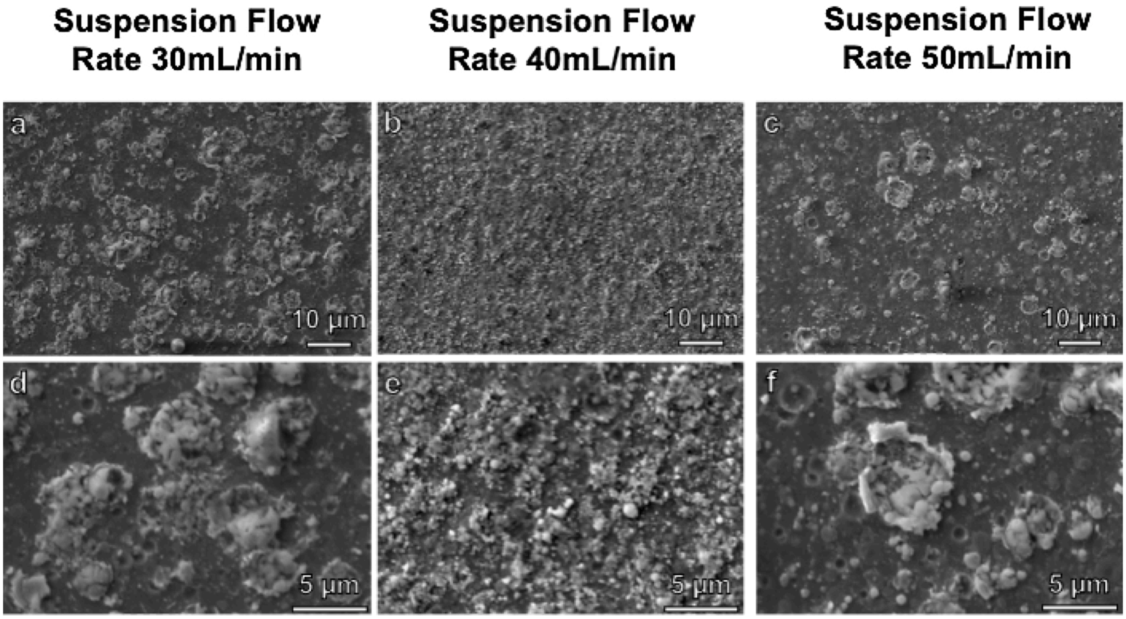

Fig. 6. Secondary Electron (SE)-SEM images for swipe test at three different flow rates (a) 30 mL/min – FLR30, (b) 40 mL/min – FLR40 and (c) 50 mL/min – FLR50, respectively, being images d to f at high magnification. All images were taken at 15 kV.

Table 2
The area coverage of the splats for a feeding rate of 30 mL/min, 40 mL/min and 50 mL/min respectively.

Feeding Rate (mL/min)	Area coverage (%) (ImageJ)
30	38.4 ± 3.1
40	67.8 ± 4.2
50	31.8 ± 2.6

40 mL/min (FLR40) as the substrate is almost fully covered with splats. At the flow rate of 30 mL/min (FLR30), shown in Fig. 6a (a higher magnification in Fig. 6d), there is a number of broken shells observed at the surface of the substrate. A small number of round particulates accompanies these broken shells As the flow rate increases to 40 mL/min (FLR40), shown in Fig. 6b (a higher magnification in Fig. 6e), the surface of the substrate comprises a mixture of molten splats and partially molten particulates. There is a minority of broken shells collected at the surface of the substrate. Instead of broken shells, the substrate is mainly covered by re-solidified agglomerates and partially molten particles. At the flow rate of 50 mL/min (FLR50), shown in Fig. 6c (a higher magnification in Fig. 6f), molten splats and a small number of partially molten particles are collected on the surface of the substrate.

Moreover, the fractured shell morphologies are mainly due to the dilute solutions used in the study, which results in surface precipitation of droplets. The surface precipitation will initiate the formation of a hard thin shell on the surface, which will fracture upon hitting the substrates. The presence of these broken shells could yield poor quality coatings, which could affect the thermal cycling performance of the coating

Table 3
EDX analysis of the cross-section of the thermally cycled S-HVOF YSZ and SP-HVOF GZ/YSZ showing atomic % of elemental composition.

Elements	S-HVOF YSZ spectra			SP-HVOF GZ/YSZ spectra		
	1	2	3	4	5	6
O	–	63.0	65.5	–	61.4	63.6
Al	7.6	36.6	19.6	6.4	36.3	19.8
Y	–	0.2	–	–	–	–
Ti	0.6	–	–	0.6	–	–
Cr	22.4	0.1	4.8	23.0	0.7	5.7
Fe	7.2	–	–	7.0	0.2	–
Co	22.5	0.1	5.7	23.5	0.5	6.6
Ni	37.8	0.1	4.4	37.8	0.8	4.3
Nb	2.1	–	–	1.8	–	–
Total	100.0	100.0	100.0	100.0	100.0	100.0

Table 4
EDX analysis of the cross-section of the thermally cycled SP-HVOF GZ/YSZ showing atomic % of elemental composition near the GZ/YSZ interface.

Elements	SP-HVOF GZ/YSZ spectra				
	1	2	3	4	5
C	24.4	24.6	25.2	25.3	23.6
Y	–	–	0.3	0.6	0.9
Zr	4.9	5.2	6.0	7.0	8.9
Gd	4.8	4.2	2.2	0.6	0.2
O	65.9	66.0	66.3	66.5	66.5
Total	100.0	100.0	100.0	100.0	100.0

[45–47].

3.3. *Thermal spray coating deposition and microstructural characterisation for both SHVOF YSZ and SP-HVOF GZ*

In this study, two types of coatings were produced: a single-layer YSZ, and double-layer GZ/YSZ. Both topcoats were deposited with the same parameters: Stand-off distance at 85 mm and the flow rate of feedstocks at 40 mL/min. These parameters were chosen resulting from the splat test discussed in the previous section (i.e., Section 3.2). A SOD of 85 mm provides the optimum distance, which is capable of providing a sufficient dwell time to melt the entrained particles prior to the deposition, whereas FLR40 was chosen because the deposition rate was significantly higher, and the heat transfer to each individual droplets was sufficient to melt all entrained solid particles.

SEM micrographs for the cross-section of the single-layer S-HVOF as-sprayed YSZ coating are presented in Fig. 7. The average thickness for the bond coat is 130 ± 10 µm, whereas the average thickness for the topcoat YSZ is 40 ± 5 µm. The deposited coating presented numerous vertical cracks (circled in red) throughout, which is observed to originate at the surface (Fig. 7a). The YSZ layer topcoat seems to be dense with a number of micropores. These micropores are seen to be uniformly distributed throughout (Fig. 7b and Fig. 7c).

Additionally, Fig. 8 represents the cross-section of the double-layer S-HVOF as-sprayed YSZ/GZ coating. The average thickness for the bond coat is 100 ± 10 µm, whereas the average thickness for the YSZ is 40 ± 5 µm and the average thickness for the solution precursor GZ is 40 ± 5 µm, implying that the ratio thickness of YSZ to GZ is evidenced to be 1 to 1. Lee et. al. claimed that the stress state of a double-layer coating design was not sensitive to the ratio thickness of the two coating layers; however, the ideal ratio of 1:1 has the capability to prevent coating failure by alleviating compressive stress that present in the coating structure [14, 48]. The stress on the surface of the second layer (bottom layer, i.e., YSZ in this study) was reported to be lower than other stresses in the coating structure [48]. The ratio thickness between the two coating layers could also be adjusted easily by changing the number of passes during deposition. Additionally, Mahade et. al. [27] presented that the double-layer TBC with a ratio thickness of 1:1 has the highest lifetime as compared to other thickness ratios.

On the other hand, both deposited YSZ and GZ layers are very dense. The vertical cracks in the YSZ layer are less pronounced here, and these stopped at the GZ layer. According to Xie et. al. [49], it was reported that the formation of vertical cracks only occurred in thick SP coatings (i.e., > 100 µm). In a thick coating deposition process, the coating temperature is higher due to a longer spraying time, subsequently leading to a

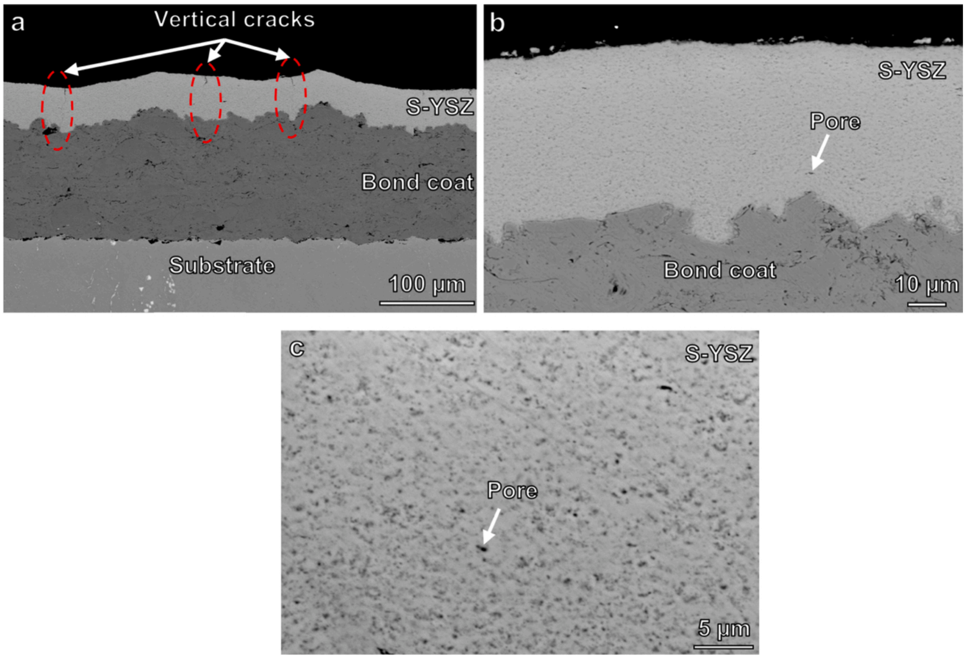

Fig. 7. (a) Cross-sectional micrographs of the single-layer Suspension HVOF as-sprayed YSZ coating generated at a stand-off distance of 85 mm and a suspension flow rate of 40 mL/min. (b) A high magnification of S-HVOF topcoat showing the interface of topcoat is well-bonded with the MCrAlY bond coat. (c) A high magnification showing that the pores are observed to be uniformly distributed throughout the coating microstructure.

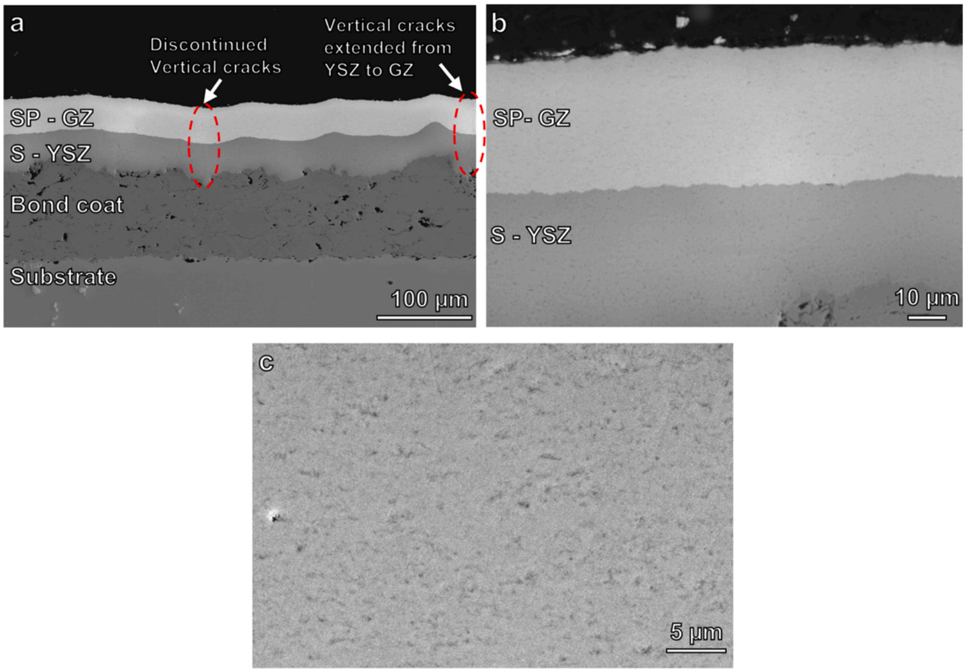

Fig. 8. (a) Cross-sectional micrographs of the double-layer HVOF as-sprayed GZ/YSZ coatings generated at a stand-off distance of 85 mm and a suspension flow rate of 40 mL/min. (b) A higher magnification of SP-HVOF GZ topcoat and the interface with the S-HVOF YSZ. (c) A higher magnification at the GZ layer, indicating a low number of pores in the GZ layer.

generation of higher tensile stresses. Although the substrates are continuously cooled externally, the number of passes of the torch contributes directly to increasing coating temperature. Vertical cracks formed as soon as these stresses exceeded the tensile strength of the coating. In this study, the coating thickness of the SP GZ is 40 ± 5 µm. Hence the generated tensile stress in the coating is not enough to initiate the propagation of vertical cracks. Moreover, the smaller splat size of the SP as compared to suspension feedstock could effectively prevent the propagation of vertical cracks from the S-YSZ. The SP coating is typically dense and well-bonded due to the smaller splats. Only a very small number of vertical cracks continued to propagate to the GZ top layer from the S-YSZ layer despite GZ having a lower fracture toughness.

Moreover, the adhesion between the SP-HVOF GZ layer and the S-HVOF YSZ layer appears to be good, with no apparent pores or gaps at the interface.

3.4. *X-ray diffraction of coatings*

The combined XRD pattern for the dried YSZ powder from the suspension, as-sprayed and heat-treated YSZ coatings is presented in Fig. 9 (a), whereas Fig. 9(b) presented a detailed peak in the range of 72 ° to 76 °. The XRD results indicate that the dried YSZ suspension powder mainly presents a tetragonal YSZ (PDF Card #00-048-0224) phase with the presence of some monoclinic zirconium oxide (PDF Card #00-078-0047). The crystalline phase for both the as-sprayed and heat-treated coating are similar to the dried YSZ suspension powder. Both as-sprayed and heat-treated coatings showed the same crystalline YSZ (PDF Card #00-048-0224) phase; however, the monoclinic zirconium oxide was not detected (shown in Fig. 9b), and some traces of yttrium oxide (PDF Card #00-047-1274) were detected (Fig. 9a). The absence of the monoclinic zirconium oxide in the resulting coating suggested that the temperature of the particles reached during the deposition process were high enough to induce the complete melt of the particles. As soon as the molten state particles impacted onto the substrate, it experienced a rapid cooling (i.e.,~10^{6} Ks^{-1} or greater [50]) and crystallised into the tetragonal phase. The monoclinic and cubic phase formation will present only if the cooling process occurs in an equilibrium condition [8]; however, there are some segregation of yttrium oxide observed due ot an inhomogeneous distribution of the yttrium oxide in the YSZ structure.

The XRD result for the as-sprayed and heat-treated double-layer GZ/YSZ coating is presented in Fig. 10. Comparing with Fig. 4, the diffractograms have the same GZ crystalline phase (PDF Card #00-080-0471), the metastable fluorite phase. This suggested that the chosen parameters (i.e., stand-off distance, flame power and suspension flow rate) were efficient to deposit the GZ as the only crystalline phase despite the complicated physical and chemical reactions associated with the precursor pyrolysis.

Moreover, the narrower peaks on the 2 h heat-treated coatings in both Figs. 9 and 10 evidenced that the coating has a larger crystallite size due to the growth of nano-crystallites induced from the heat-treatment [30].

3.5. *Thermal cycling test*

Referring to Fig. 12, the average thermal cycle to failure for the single-layer YSZ is 85 ± 5 cycles, whereas for the double-layer GZ/YSZ is 70 ± 15 cycles. Fig. 11 represents the surface morphology of the coatings after thermal cycling test at 25 cycles, 55 cycles, 70 cycles, and 85 cycles, respectively. The failure for both samples initiated from the edges and propagated to the center of the samples. Both samples failed at the bond coat/topcoat interface because the bond coat surface (blue colour region) is exposed, as shown in Fig. 11. The thermal cycling performance of both TBC samples seems the same as each other. The only difference is that the double-layer GZ/YSZ has a smaller area exposure of bond coat (20 %) than the single-layer YSZ,~24 % area spallation.

The cross-sectional SEM micrographs of the failed samples are shown in Fig. 13. The failure of the single-layer YSZ occurred at the topcoat (YSZ) and TGO interface, as seen in Fig. 13 (a) and (b), whereas the failure of the double-layer GZ/YSZ occurred at the topcoat (YSZ) and TGO interface as well as the GZ layer near to the interface with YSZ layer, as seen in Fig. 13 (c) and (d). Moreover, the horizontal crack was observed to propagate from the YSZ layer to the GZ layer Fig. 13(d).

The XRD analysis of the single-layer YSZ and double-layer GZ/YSZ thermal cycled samples are shown in Figs. 14 and 16, respectively. The

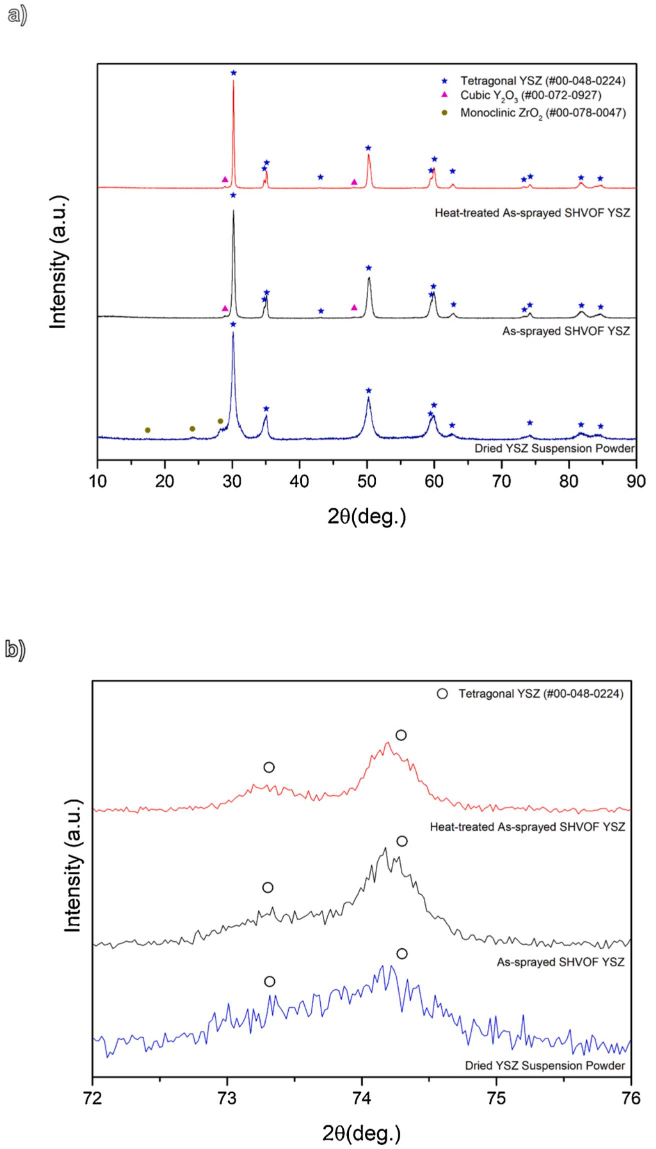

Fig. 9. (a) XRD result of the dried YSZ suspension powder, SHVOF as-sprayed single-layer YSZ and the heat-treated as-sprayed YSZ coating. (b) A detailed view of the range of interest, 72 ° - 76 °, for phase identification. No monoclinic zirconium oxide peaks are seen in the as-sprayed TBC sample.

XRD patterns of each sample before the thermal treatment are depicted for comparison purposes. The thermal cycled single-layer YSZ sample shows that tetragonal YSZ is the main crystalline phase (PDF Card #00-048-0224) as it was also presented in the sample before thermal cycling. Some amounts of monoclinic zirconium oxide (PDF Card #00-078-0047) and cubic yttrium oxide (PDF Card #00-072-0927) are detected; however, the presence of monoclinic zirconium oxides is minimal. Besides, the Co-alloy from the bond coat is detected (PDF Card #00-035-1489) along with aluminum oxides (corundum, PDF Card #00-046-1212) and cobalt aluminum oxides (spinel, PDF Card #00-082-2251) which were formed as TGO layer, resulting from the oxidation of the bond coat.

The thermal cycled double-layer GZ/YSZ sample showed some GZ (PDF Card #00-080-0471) peaks, as detected in the sample before the thermal treatment; however, the tetragonal YSZ from the bottom layer coating represents the main crystalline phase (PDF Card #00-048-0224) and a gadolinium yttrium oxide phase (PDF Card #00-081-2218) is newly formed. The traces of the gadolinium yttrium oxide phase suggested that some of the gadolinium cations (Gd) may have diffused into the YSZ layer [51]. A higher magnification SEM image showed that porosities occured in the GZ layer near the GZ/YSZ interface (Fig. 18) were the consequences of Gd diffusions, which also reported in [51]. The event of Gd diffusion seemed to happen locally because in some regions, cracks could have grown before extensive Gd diffusion occurs. Designated white spots placed at the region (Spectrum 1 to Spectrum 5) are believed to have Gd diffusion into the YSZ layer for EDX analysis, where traces of Gd elements are found in the YSZ layer. Moreover, SEM images were taken after the sample had failed; hence the event of Gd diffusion into the YSZ layer would required additional investigation. Meanwhile, the bond coat alloy is also detected (PDF Card #00-035-1489) along with aluminium oxides (corundum, PDF Card #00-046-1212) and cobalt aluminium oxides (spinel, PDF Card #00-082-2251), resulting from the oxidation of bond coat. Apart from the peaks obtained from XRD, EDX analysis also suggested the same compositions around the TGO region for both samples, as shown in Figs. 15 and 17.

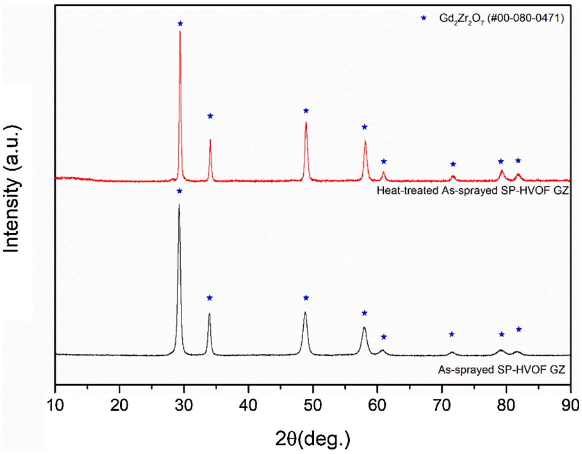

Fig. 10. XRD result of the SHVOF as-sprayed double-layer GZ/YSZ as well as the heat-treated as-sprayed coating.

4. Discussion

4.1. Thermal characteristics of GZ precursor

It is essential to understand the thermal behaviour of the GZ solution precursor to ensure that the chosen spray parameters (i.e., flame powder) are sufficient to deposit a crystalline GZ coating. The SDT data (i.e., Fig. 3) suggested that the sharp endothermic peak at ~104 °C corresponds to the highest heat energy absorbed by the solution precursor feedstock as soon as injected into the combustion flame. Due to the predominantly endothermic behaviour of the solution precursor, the flame temperature is expected to be lower. The heat transferred from the flame will first be required to evaporate the solvent medium (water), which then transform to form particles in flight. As soon as the in-flight particle temperature reached 350 °C, a small amount of heat energy was released into the system (two exothermic peaks represented a combination of endothermic and exothermic behaviour of acetates and nitrates), indicating that organic compounds' decomposition is completed, leaving only GZ particles in flight.

As compared to powder or suspension feedstocks, the solution precursor feedstock cooled down the flame as it enters into the HVOF flame, causing the formation and melting of particles to occur at a location further down the gas stream. A further decrement in the gas temperature is expected as the distance away from the torch increases. Beyond the critical location in the flame, the gas temperature dropped below the melting point of the materials, and some of the entrained particles will never be melted [52]. Instead of depositing on the substrates, these un-pyrolysed particles will either flow off the gas stream or bounce off from the substrates.

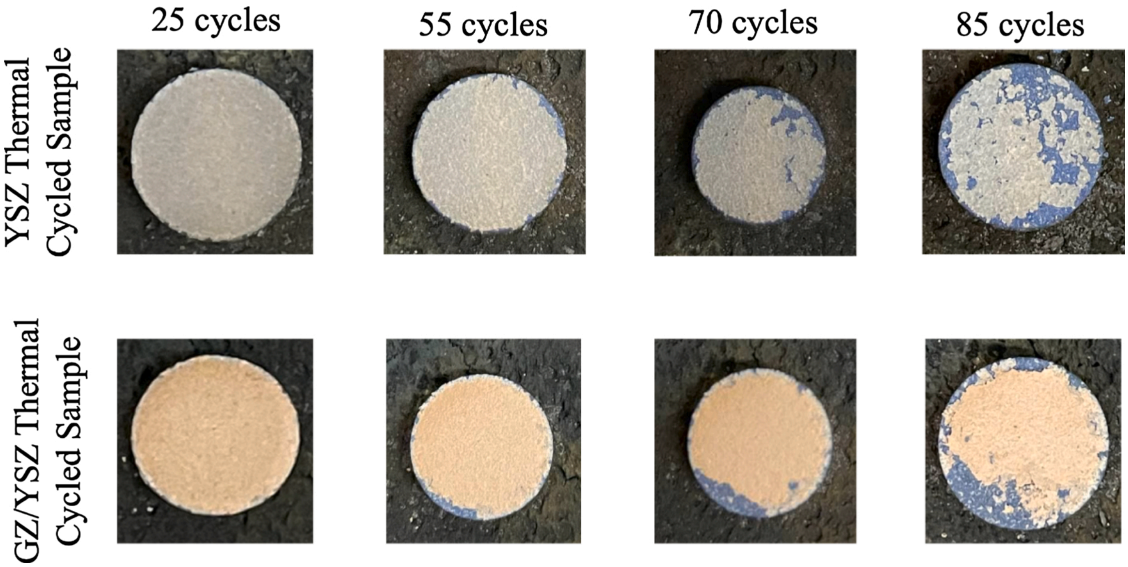

Fig. 11. Surface morphology of thermal cycled samples at 25 cycles, 55 cycles, 70 cycles, and 85 cycles, respectively.

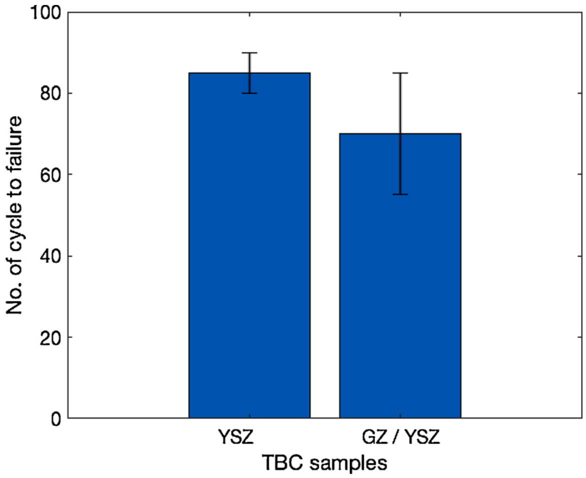

Fig. 12. Summary of thermal cyclic durability of TBC samples, consisting of single-layer YSZ and double-layer GZ/YSZ TBCs (4 samples were tested for each group).

Despite the event of melting GZ particles occurring later in the flame section, the XRD results (i.e., Figs. 4 and 10) showed completely crystalline phases present in the coating. It is evidenced that the chosen power for the HVOF process was more than enough to evaporate the liquid medium and decompose the precursors, following the melting of the particles in the combustion flame and rapid quenching of the particles that crystallised as GZ phase.

4.2. Splat formation

In previous studies [45,53], it was found that the stand-off distance (SOD) and the flow rate (FLR) of feedstocks have a strong effect on coating properties. This section will focus on the analysis of how these variables affect the deposition of GZ.

SOD in thermal spray determines the distance of particles before impacting on the substrate surface to form a layer of coating as splats. The dwell time of particles in the flame is directly affected by varying the SOD. At a shorter distance (i.e., SOD75), the particle experienced a shorter amount of time in the flame. As soon as the particle experienced pyrolysis and sintering, the particle impacted the substrate. The short dwell time in the flame has significantly reduced the heat transfer to each particle, resulting in a low degree of molten splats; however, the flame temperature is high enough to pyrolyse and sinter all in-flight particles. It is evidenced by the individual solid particulates and agglomerated solid particles on the surface of the substrate (Fig. 5a and d). The formation of agglomerated solid particles is due to larger initial droplets that experience a higher heating transfer [53].

By increasing the SOD to 85 mm (i.e., SOD85), the dwell time of particles in the flame is significantly improved. Although the flame temperature is lower due to an increment in the distance away from the torch, the in-flight particles experienced a higher heat transfer. The in-flight particles are re-heated and re-melted, then impacts onto the surface of the substrate, yielding a higher degree of molten splats (as evidenced in Fig. 5b and e). As the particles remained longer in the flame (i.e., SOD95), the in-flight particles continued heating and undergoing an additional tertiary fragmentation process [53], in which the particles break up into a smaller size that may not be able to stay in the trajectory within the flame (as evidenced in Fig. 5c and f).

The flow rate (FLR) of feedstocks in thermal spray determines the amount of solution precursor being injected into the flame per minute. The amount of solution precursor dictates the number of particles being heated once it enters the HVOF flame. At a low flow rate (FLR30), the amount of solvent needed to evaporate is much lower, resulting in heating solid particles occurring at a much earlier stage and experienced a higher heat transfer. The longer dwell time of materials in the flame led to a fully molten splat on the surface of the substrate (Fig. 6a and d). Increasing the flow rate to FLR40 resulted in more energy and time are needed to evaporate the solvent, consequently delaying the heating of particles and a cooler flame. Although the dwell time of particles is now reduced, it is still enough to melt most of the entrained particles into a molten state; however, a small number of particles that are only experiencing pyrolysis and sintering will appear as partially molten particles or agglomerations (Fig. 6b and e), depending on the size of the droplets. As more solution precursors (FLR50) being injected into the flame, the time for the supplied heat energy to evaporate the medium is much longer. Consequently, the heating of particles will only occur further down the gas stream (away from the torch), resulting in a much cooler flame which significantly affects the heat transfer from the flame to each in-flight particle. The low deposition efficiency suggested that some of the un-pyrolysed particles either failed to follow the flight trajectory or bounced off from the substrates.

In addition, the behaviour of a liquid during atomisation is usually described with the dimensionless Weber number, *We*, and Reynolds

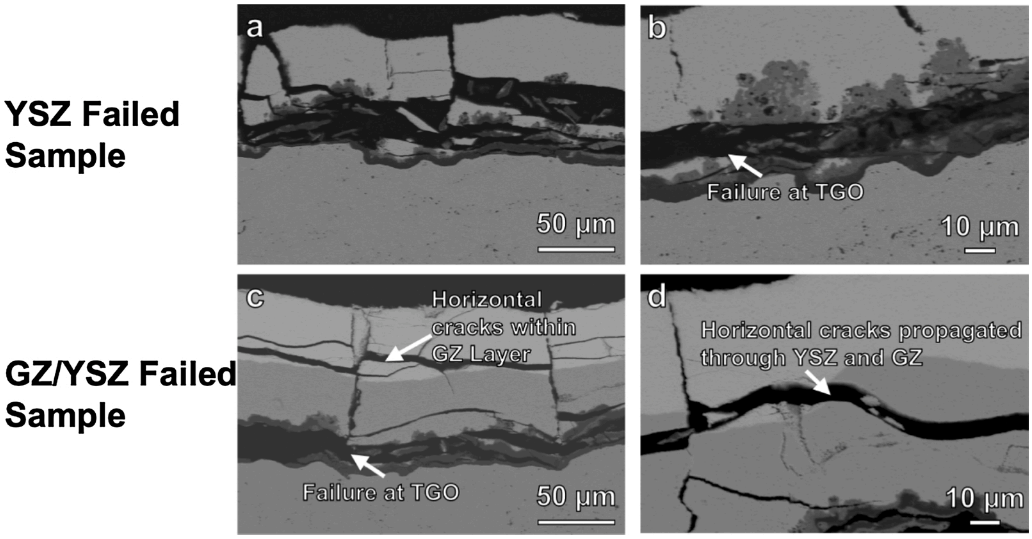

Fig. 13. Comparison of the thermal cycle failure mechanism between the single-layer YSZ and double-layer GZ/YSZ samples. (a) SEM micrograph of the failed YSZ sample (b) A higher magnification of failure near bond coat. (c) SEM micrograph of the failed GZ/YSZ sample. (d) A higher magnification of failure at the interface of GZ and YSZ, showing that horizontal crack propagated through YSZ and GZ layer.

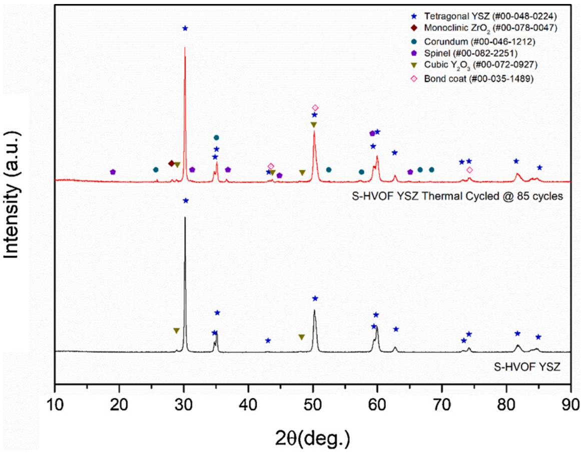

Fig. 14. XRD result of the as sprayed and the thermal cycled S-HVOF YSZ sample at 1135 °C.

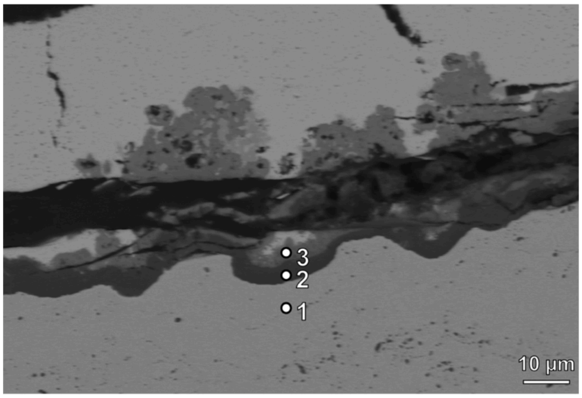

Fig. 15. SE-SEM micrograph showing the thermal cycled S-HVOF YSZ topcoat respectively with the TGO layer with white dots designating EDX spectrum collection spots (see Table 3).

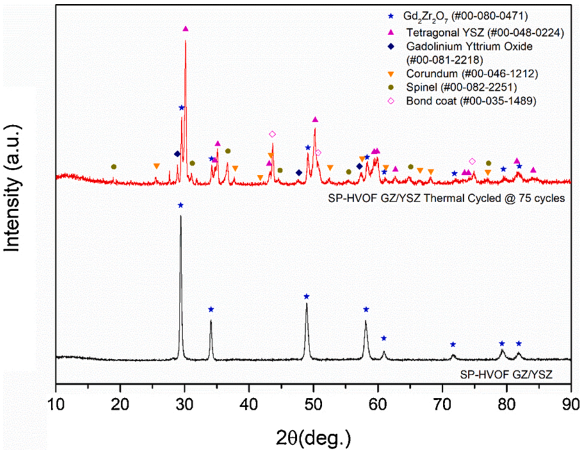

Fig. 16. XRD result of as sprayed and the thermal cycled SP-HVOF GZ/YSZ sample at 1135 °C.

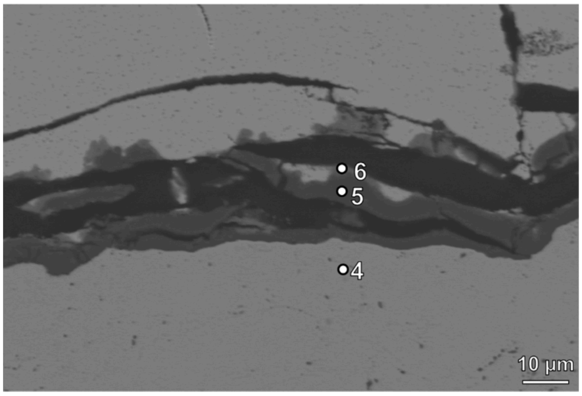

Fig. 17. SE-SEM micrograph showing the thermal cycled SP-HVOF GZ/YSZ topcoat respectively with the TGO layer with white dots designating EDX spectrum collection spots (see Table 3).

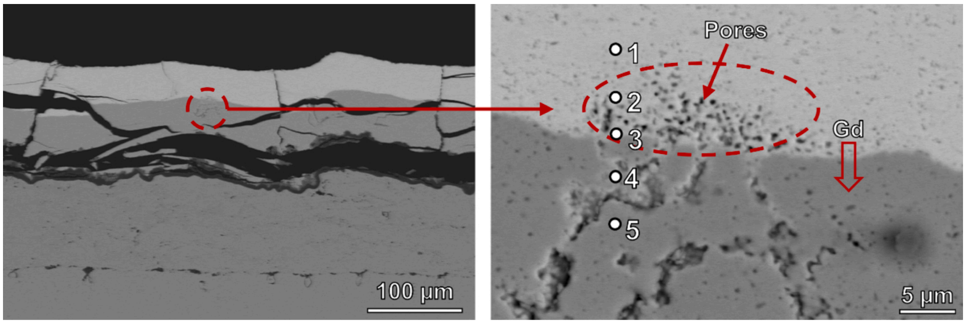

Fig. 18. SE-SEM micrograph showing pores in GZ layer near the GZ/YSZ interface. The pores suggested that Gd diffused into the YSZ layer to form the new oxide, gadolinium yttrium oxide. The designated white dots showed the EDX spectrum collection spots (see Table 4).

number, *Re*. *We* number is the ratio of the deforming intertia force of the medium to the surface tension of the droplet whereas *Re* number is the ratio of fluid inertia to viscosity [30]. The solution precursor used in this study is a water-based precursor, which the *Re* value is in the range of 1500 and *We* value is in the range of 15 [30,54]. According to the simulation study run by Sunil et. al. [55], the water-based feedstock will result in a larger droplet associated with a dense coating (Fig. 8c)."

4.3. Microstructure of as-sprayed coating

The S-HVOF YSZ TBCs were optimised and discussed previously in our publications for prominent vertical cracks and low porosities [30, 38]. The repeatability of microstructures is proven viable (Fig. 7). This section is going to focus on solution precursor spraying of GZ.

The top layer, SP-HVOF GZ, was deposited using 101 kW flame power (see Table 1). It presents a considerably dense coating microstructure with occasional vertical cracks (Fig. 8a) extended from the S-HVOF YSZ layer. The produced coating structures indicated that the heat transfer in-flight is enough to melt most sintered particles. The vertical cracks that were observed in the single-layer S-YSZ were mainly due to the tensile stress presents in the coating structure, acting as the main driving force for the generation of vertical cracks; however, the solution precursor GZ produces a smaller splat size and denser coating structure as compared to the suspension feedstock used in the YSZ layer (Fig. 8c). Additionally, the high degree of molten splats successfully covered the spaces between the splats, effectively blocking the cracks to

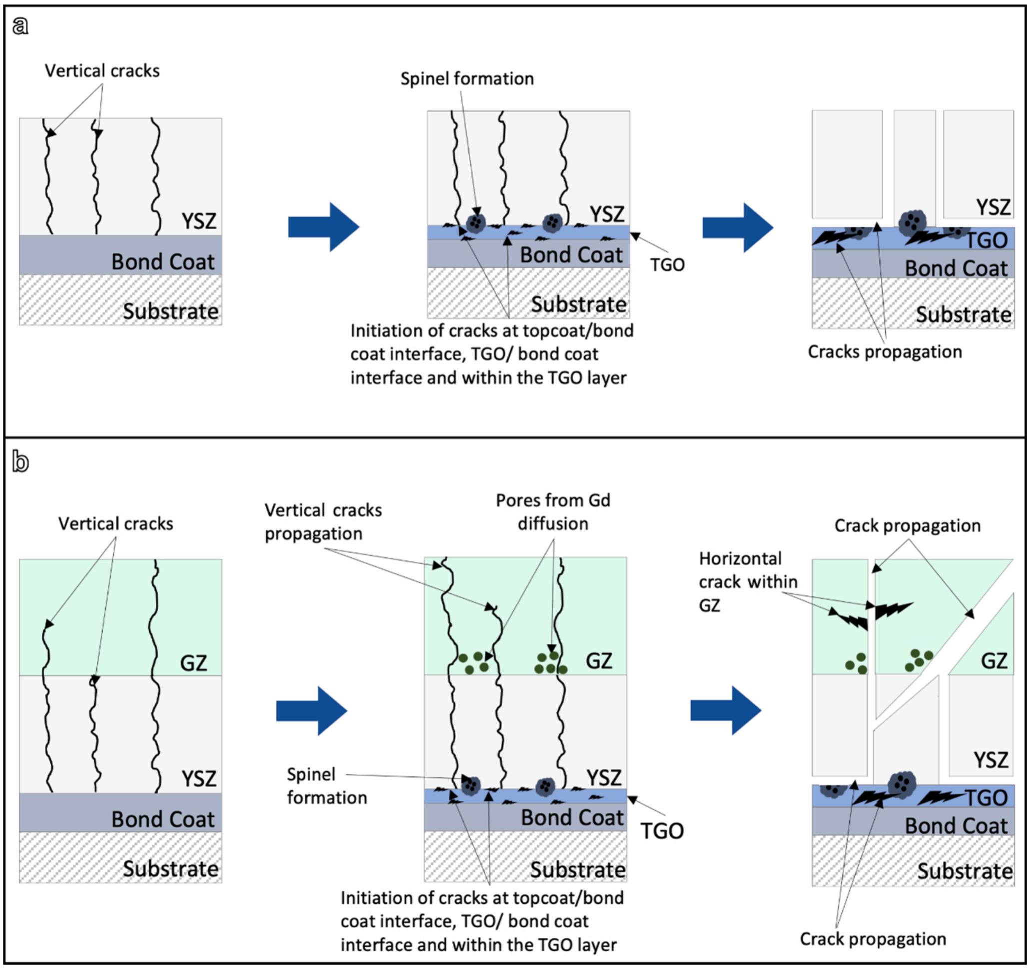

Fig. 19. (a) Crack sequence for the single-layer YSZ (b) Crack sequence for the double-layer GZ/YSZ.

propagate from the S-HVOF YSZ layer. The vertical cracks propagated from the YSZ layer to the top surface of the GZ layer could be due to the partially molten or agglomerated particles (Fig. 6b and 6e); however, these vertical cracks are found occasionally.

Moreover, an experimental study for the same flame power (101 kW) at 85 mm SOD and 50 mL/min suspension FLR shows that the temperature of the in-flight molten particles for the solution precursor feedstock is lower than the suspension feedstock [56]. The lower in-flight temperature seems to be caused by the predominant endothermic behaviour of the solution precursor, resulting in the melting process of the in-flight particles which start much later down the gas stream and significantly decreasing the dwell time for the solid particles [52].

4.4. Failure modes

The single-layer YSZ has a different failure mode to the double-layer GZ/YSZ. The single-layer YSZ failed primarily in the topcoat/TGO interface. Fig. 19(a) shows a schematic diagram of the crack growth in the single-layer YSZ TBC. Initially, TGO starts to grow at the topcoat/bond coat interface and multiple cracks begin to form at the region near topcoat/TGO interface or within the TGO [57]. As thermocycling continues, these cracks grow, and vertical cracks (obtained from the as-sprayed condition) start to widen [58]. Echsler et al. [57] reported various types of cracks that can form in the vicinity of the TGO prior to TBC's failure. Cracks initiated within the TGO (defined as Type B) and cracks that started and penetrated the topcoat (defined as Type D) are the most common cracks seen in thermal cycled samples. In contrast, cracks in the vicinity of areas with a non-ideal bond coat surface finish (defined as Type A) and cracks located at the TGO/bond coat interface (defined as Type C) are less common to be seen.

The vertical cracks, also known as the stress-relieving cracks that are already present in coating microstructure after deposition, can be the crack initiation site due to the thermal mismatch between the topcoat and the substrate. According to Naumenko et. al., the driving force for crack initiation and propagation in the vicinity of TGO is also linked to the thermal mismatch between the topcoat and substrate [59]. The inevitable growth of TGO increases its thickness over time, resulting in a volume expansion in the coating structure and the development of compressive stresses in the TGO upon cooling. These compressive stresses developed in the TGO were shown to cause the failure [6].

Moreover, the formation of less protective oxides, spinel (appears in a lighter contrast than Al_2O_3), start to form at regions adjacent to the topcoat/TGO interface in clusters (Fig. 13(a) and 13 (b)). Interestingly, spinels are mainly formed at the region connected to cracks in the topcoat, suggesting that regions with higher oxygen partial pressure (regions with crevices) favour spinel formation [60]. The presence of spinels is believed to induce stresses in the coating structure due to the large volume change as a result of the formation of oxides at the topcoat/TGO interface [57,60], initiating or helping crack propagation at the topcoat/TGO interface, and subsequently, the coating spalled off.

Compared to the single-layer YSZ, the double-layer GZ/YSZ TBCs have a much complicated failure mode, where the horizontal cracks seen to propagate within the GZ layer (Fig. 12(c)) and through the GZ/YSZ layer. The initial crack growth stage is similar to the single-layer YSZ TBC, where TGO and cracks seem to form (Fig. 19(b)). By increasing the number of thermocycling, the vertical cracks in the YSZ layer widen, and the vertical cracks start to extend to the top surface of the GZ layer. With the long hours of exposure, Gd cations begin to diffuse into the YSZ layer to form gadolinium yttrium oxide (PDF #00-081-2218), represented in the XRD peaks (Fig. 16) and EDX analysis (Fig. 18). The diffusion of Gd leads to an increase in porosities on both the Gd and YSZ layers, which may be helpful for thermal cycling performance [51]; however, the formation of the new phase, gadolinium yttrium oxide, imposing a volume change of approximately 13.7 % in the coating structure, inducing more stresses and subsequently initiating horizontal crack propagation through the GZ/YSZ layer. Meanwhile, horizontal cracks in the region where no Gd diffusion occurred is mainly due to the lower fracture toughness in the GZ layer [58].

5. Conclusion

This paper presents the successful production of GZ coatings from solution precursor and provides a comparison between the single-layer S-HVOF YSZ coating and the double-layer SP-HVOF GZ/YSZ coating for the first time. The inevitable growth of TGO that increases in thickness over time is one of the main factors to cause coating spallation. The higher the TGO growth rate, the shorter the lifetime of TBCs. In thermal cycling, the TGO releases strain energy (out of plane displacements) into the bond coat. As soon as the stored energy at the interface exceeds the threshold value, cracks and coating spallation occurs. Owing to the thermal expansion mismatch between the topcoat and substrate, the already present stress-relieving cracks or known as vertical cracks, can be the crack initiation sites. In the cooling phase, the thermal mismatch between the topcoat and substrate also plays an important role in the crack initiation and propagation at areas adjacent to the TGO. The thermal cycling performance of both coatings was compared. The following conclusions can be drawn:

- The SP GZ reaction was predominantly governed by an endothermic behaviour followed by exothermic reactions to decompose all organic compounds present in the solution (i.e., gadolinium nitrate and zirconium acetate). It was also proven that the GZ crystalline phase starts to form after 800 °C, indicating GZ crystalline structure present in the deposited coating.
- The solution precursor GZ was successfully employed in this study to deposit a double-layer GZ/YSZ topcoat by HVOF thermal spray. The optimised spray parameters were sufficient to melt all the entrained solid particles, producing a dense coating structure in the GZ layer.
- The single-layer failed at the topcoat/TGO interface, whereas the double-layer GZ/YSZ failed at GZ/YSZ interface and topcoat/TGO interface.
- In the thermally cycled samples, horizontal cracks that were observed in the double-layer GZ/YSZ sample initiated from the YSZ layer. Gd diffusion took place near the GZ/YSZ interface, resulting in porosities in the GZ layer. The formation of new phases, gadolinium yttrium oxide, will lead to 13.7 % volume change in the coating structure. The volume change is believed to introduce cracks into the system, subsequently leading to coating failure. In the region where no Gd diffusion has occurred, the horizontal crack propagation within the GZ layer is mainly due to the lower fracture toughness in the GZ layer.

6. Future work

Optimisation of the GZ layer in the double-layered TBCs is needed to improve the durability of the GZ layer by implementing sufficient amounts of porosities in the coating structure and increasing the coating thickness.

Data availability

No data was used for the research described in the article.
Data will be made available on request.

Declaration of Competing Interest

The authors declare that they have no known competing financial interests or personal relationships that could have appeared to influence the work reported in this paper.

Acknowledgements

This work was supported by the Engineering and Physcial Sciences Research Council (ESPRC) (grant number EP/R511730/1). The authors would like to thank John Kirk for his assistance during the SSP-HVOF thermal spray. The authors acknowledge the Nanoscale and Microscale Research Centre (nmRC) at the University of Nottingham for access to the SEM, FEG-SEM and Raman spectroscopy facilities.

References

[1] W.R. Group, High Temperature Coatings, University of Virginia, 2013.
[2] W.J. Brindley, Thermal barrier coatings of the future, J. Therm. Spray Technol. 6 (no. 1) (1997) 3–4.
[3] R.A. Miller, Thermal barrier coatings for aircraft engines: history and directions, J. Therm. Spray Technol. 6 (1) (1997) 35–42.
[4] X.Q. Cao, R. Vassen, D. Stoever, Ceramic materials for thermal barrier coatings, J. Eur. Ceram. Soc. 24 (no. 1) (2004) 1–10.
[5] W. Pan, S.R. Phillpot, C. Wan, A. Chernatynskiy, Z. Qu, Low thermal conductivity oxides, MRS Bull. 37 (no. 10) (2012) 917–922.
[6] T.M. Pollock, D.M. Lipkin, K.J. Hemker, Multifunctional coating interlayers for thermal-barrier systems, MRS Bull. 37 (no. 10) (2012) 923–931.
[7] N.P. Padture, M. Gell, E.H. Jordan, Thermal barrier coatings for gas-turbine engine applications, Science 296 (no. 5566) (2002) 280–284, 80.
[8] N.L. Ndamka, Microstructural Damage of Thermal Barrier Coatings Due To CMAS Attack, Cranfield Univeristy, 2013.
[9] J. Torres-Rodriguez, et al., Rare-earth zirconate Ln2Zr2O7 (Ln: La, Nd, Gd, and Dy) powders, xerogels, and aerogels: preparation, structure, and properties, Inorg. Chem. 58 (21) (2019) 14467–14477.
[10] S. Mahade, N. Curry, S. Björklund, N. Markocsan, P. Nylén, Failure analysis of Gd2Zr2O7/YSZ multi-layered thermal barrier coatings subjected to thermal cyclic fatigue, J. Alloys. Compd. 689 (2016) 1011–1019.
[11] M. Guven Gok, G. Goller, State of the art of gadolinium zirconate based thermal barrier coatings: design, processing and characterization, Methods Film Synth. Coat. Proced. (2020).
[12] S. Krämer, J. Yang, C.G. Levi, C.A. Johnson, Thermochemical interaction of thermal barrier coatings with molten CaO-MgO-Al 2O 3-SiO 2 (CMAS) deposits, J. Am. Ceram. Soc. 89 (no. 10) (2006) 3167–3175.
[13] S. Krämer, J. Yang, C.G. Levi, Infiltration-inhibiting reaction of gadolinium zirconate thermal barrier coatings with CMAS melts, J. Am. Ceram. Soc. 91 (no. 2) (2008) 576–583.
[14] C. Jiang, E.H. Jordan, A.B. Harris, M. Gell, J. Roth, Double-Layer Gadolinium Zirconate/Yttria-Stabilized Zirconia Thermal Barrier Coatings Deposited by the Solution Precursor Plasma Spray Process, J. Therm. Spray Technol. 24 (no. 6) (2015) 895–906.
[15] E.M. Zaleski, Mitigation of CMAS Attack on Thermal Barrier Coatings, no. March, 2013.
[16] T. Steinke, D. Sebold, D.E. Mack, R. Vaßen, D. Stöver, A novel test approach for plasma-sprayed coatings tested simultaneously under CMAS and thermal gradient cycling conditions, Surf. Coatings Technol. 205 (no. 7) (2010) 2287–2295.
[17] E. Bakan, D.E. Mack, G. Mauer, R. Vaßen, Gadolinium zirconate/YSZ thermal barrier coatings: Plasma spraying, microstructure, and thermal cycling behavior, J. Am. Ceram. Soc. 97 (no. 12) (2014) 4045–4051.
[18] A.U. Munawar, U. Schulz, G. Cerri, H. Lau, Microstructure and cyclic lifetime of Gd and Dy-containing EB-PVD TBCs deposited as single and double-layer on various bond coats, Surf. Coatings Technol. 245 (2014) 92–101.
[19] M. Frommherz, A. Scholz, M. Oechsner, E. Bakan, R. Vaßen, Gadolinium zirconate/YSZ thermal barrier coatings: mixed-mode interfacial fracture toughness and sintering behavior, Surf. Coatings Technol. 286 (2016) 119–128.
[20] A. Ganvir, et al., Design of thermal barrier coatings, Model. Approach 220 (1–2) (2015).
[21] S. Mahade, N. Curry, S. Björklund, N. Markocsan, P. Nylén, R. Vaßen, Functional performance of Gd2Zr2O7/YSZ multi-layered thermal barrier coatings deposited by suspension plasma spray, Surf. Coat. Technol. 318 (2017) 208–216.
[22] D. Zhou, et al., Thermal cycling performances of multilayered yttria-stabilized zirconia/gadolinium zirconate thermal barrier coatings, J. Am. Ceram. Soc. 103 (no. 3) (2020) 2048–2061.
[23] S. Mahade, N. Curry, S. Björklund, N. Markocsan, P. Nylén, Thermal conductivity and thermal cyclic fatigue of multilayered Gd2Zr2O7/YSZ thermal barrier coatings processed by suspension plasma spray, Surf. Coat. Technol. 283 (2015) 329–336.
[24] K.S. Lee, D.H. Lee, T.W. Kim, Microstructure controls in Gadolinium Zirconate/YSZ double layers and their properties, J. Ceram. Soc. Jpn. 122 (1428) (2014) 668–673.
[25] R. Vaßen, et al., Performance of YSZ and Gd2Zr2O7/YSZ double layer thermal barrier coatings in burner rig tests, J. Eur. Ceram. Soc. 40 (no. 2) (2020) 480–490.
[26] X. Zhong, et al., Thermal shock behavior of toughened gadolinium zirconate/YSZ double-ceramic-layered thermal barrier coating, J. Alloys. Compd. 593 (2014) 50–55.
[27] S. Mahade, N. Curry, K.P. Jonnalagadda, R.L. Peng, N. Markocsan, P. Nylén, Influence of YSZ layer thickness on the durability of gadolinium zirconate/YSZ double-layered thermal barrier coatings produced by suspension plasma spray, Surf. Coat. Technol. vol. 357 (October) (2019) 456–465.
[28] D.R. Clarke, C.G. Levi, Materials design for the next generation thermal barrier coatings, Annu. Rev. Mater. Res. 33 (2003) 383–417, no. Figure 2.
[29] S. Sampath, U. Schulz, M.O. Jarligo, S. Kuroda, Processing science of advanced thermal-barrier systems, MRS Bull. 37 (no. 10) (2012) 903–910.
[30] M. Bai, H. Maher, Z. Pala, T. Hussain, Microstructure and phase stability of suspension high velocity oxy-fuel sprayed yttria stabilised zirconia coatings from aqueous and ethanol based suspensions, J. Eur. Ceram. Soc. 38 (no. 4) (2018) 1878–1887.
[31] T. Owoseni, Suspension Thermal Spray of Alumina And Zirconia, 2020.
[32] A. Ganvir, N. Curry, N. Markocsan, P. Nylén, F.L. Toma, Comparative study of suspension plasma sprayed and suspension high velocity oxy-fuel sprayed YSZ thermal barrier coatings, Surf. Coat. Technol. 268 (2015) 70–76.
[33] E. Bakan, D.E. Mack, G. Mauer, R. Mücke, R. Vaßen, Porosity-property relationships of plasma-sprayed Gd2Zr2O7/YSZ thermal barrier coatings, J. Am. Ceram. Soc. 98 (8) (2015) 2647–2654.
[34] S. Mahade, N. Curry, S. Björklund, N. Markocsan, S. Joshi, Durability of gadolinium zirconate/YSZ double-layered thermal barrier coatings under different thermal cyclic test conditions, Materials (Basel). 12 (no. 14) (2019).
[35] R. Kumar, D. Cietek, C. Jiang, J. Roth, M. Gell, E.H. Jordan, Influence of microstructure on the durability of gadolinium zirconate thermal barrier coatings using APS & SPPS processes, Surf. Coatings Technol. 337 (January) (2018) 117–125.
[36] M. Gell, et al., Thermal barrier coatings made by the solution precursor plasma spray process, J. Therm. Spray Technol. 17 (1) (2008) 124–135.
[37] S. Saeidi, Microstructure, Oxidation & Mechanical Properties of As-sprayed and Annealed HVOF & VPS CoNiCrAlY Coatings, University of Nottingham, 2011.
[38] D. Tejero-Martin, M. Bai, J. Mata, T. Hussain, Evolution of porosity in suspension thermal sprayed YSZ thermal barrier coatings through neutron scattering and image analysis techniques, J. Eur. Ceram. Soc. 41 (no. 12) (2021) 6035–6048.
[39] A.C. Geiculescu, H.G. Spencer, Thermal decomposition and crystallization of aqueous sol-gel derived zirconium acetate gels: effects of the additive anions, J. Solgel Sci. Technol. 17 (1) (2000) 25–35.
[40] P. Melnikov, V.A. Nascimento, L.Z.Z. Consolo, A.F. Silva, Mechanism of thermal decomposition of yttrium nitrate hexahydrate, Y(NO3)3·6H2O and modeling of intermediate oxynitrates, J. Therm. Anal. Calorim. 111 (no. 1) (2013) 115–119.
[41] C.L.S. Silva, S.G. Marchetti, A.D.C.F. Júnior, T.D.F. Silva, J.M. Assaf, M.D. C. Rangel, Effect of gadolinium on the catalytic properties of iron oxides for WGSR, Catal. Today 213 (2013) 127–134.
[42] C.L. Wan, W. Pan, Q. Xu, C.J. Jiang, K. Mori, T. Torigoe, Synthesis of gadolinium zirconate by coprecipitaiton and its properties for TBC application, Key Eng. Mater. 280–283 (no. II) (2005) 1501–1502.
[43] S. Chadha, R. Jefferson-Loveday, F. Venturi, T. Hussain, A computational and experimental investigation into radial injection for suspension high velocity oxy-fuel (SHVOF) thermal spray, J. Therm. Spray Technol. 28 (6) (2019) 1126–1145.
[44] L. Pawlowski, Suspension and solution thermal spray coatings, Surf. Coat. Technol. 203 (19) (2009) 2807–2829.
[45] S. Govindarajan, R.O. Dusane, S.V. Joshi, Understanding the formation of vertical cracks in solution precursor plasma sprayed yttria-stabilized zirconia coatings, J. Am. Ceram. Soc. 97 (11) (2014) 3396–3406.
[46] D. Chen, E.H. Jordan, M. Gell, Effect of solution concentration on splat formation and coating microstructure using the solution precursor plasma spray process, Surf. Coatings Technol. 202 (no. 10) (2008) 2132–2138.
[47] L. Pawlowski, Finely grained nanometric and submicrometric coatings by thermal spraying: A review, Surf. Coatings Technol. 202 (no. 18) (2008) 4318–4328.
[48] D. Lee, T.W. Kim, K.S. Lee, Erratum: design of thermal barrier coatings using gadolinium zirconate ceramics: a study on gadolinium zirconate/YSZ bilayers (Journal of the Ceramic Society of Japan (2009), 117 5 (550-554)), J. Ceram. Soc. Japan 117 (1367) (2009) 856.
[49] L. Xie, et al., Formation of vertical cracks in solution-precursor plasma-sprayed thermal barrier coatings, Surf. Coat. Technol. 201 (3–4) (2006) 1058–1064.
[50] H. Xu, H. Guo, Thermal Barrier Coatings, Woodhead Publishing, 2011.
[51] A.C. Karaoglanli, K.M. Doleker, Y. Ozgurluk, Interface failure behavior of yttria stabilized zirconia (YSZ), La2Zr2O7, Gd2Zr2O7, YSZ/La2Zr2O7 and YSZ/Gd2Zr2O7 thermal barrier coatings (TBCs) in thermal cyclic exposure, Mater. Charact. 159 (December) (2020), 2019, p. 110072.
[52] C.K. Muoto, E.H. Jordan, M. Gell, M. Aindow, Identification of desirable precursor properties for solution precursor plasma spray, J. Therm. Spray Technol. 20 (no. 4) (2011) 802–816.
[53] D. Tejero-Martin, Z. Pala, S. Rushworth, T. Hussain, Splat formation and microstructure of solution precursor thermal sprayed Nb-doped titanium oxide coatings, Ceram. Int. 46 (no. 4) (2020) 5098–5108.
[54] H. Zhao, H.F. Liu, J.L. Xu, W.F. Li, K.F. Lin, Temporal properties of secondary drop breakup in the bag-stamen breakup regime, Phys. Fluids 25 (no. 5) (2013) 217–236.
[55] S. Chadha, R. Jefferson-Loveday, T. Hussain, A high-fidelity simulation of the primary breakup within suspension high velocity oxy fuel thermal spray using a coupled volume of fluid and discrete phase model, Int. J. Multiph. Flow 133 (2020) p. 103445.
[56] T.A. Owoseni, et al., YAG thermal barrier coatings deposited by suspension and solution precursor thermal spray, Ceram. Int. (May) (2021).
[57] H. Echsler, V. Shemet, M. Schütze, L. Singheiser, W.J. Quadakkers, Cracking in and around the thermally grown oxide in thermal barrier coatings: a comparison of isothermal and cyclic oxidation, J. Mater. Sci. 41 (4) (2006) 1047–1058.

[58] S. Mahade, R. Li, N. Curry, S. Björklund, N. Markocsan, P. Nylén, Isothermal oxidation behavior of Gd2Zr2O7/YSZ multilayered thermal barrier coatings, Int. J. Appl. Ceram. Technol. 13 (3) (2016) 443–450.

[59] D. Naumenko, V. Shemet, L. Singheiser, W.J. Quadakkers, Failure mechanisms of thermal barrier coatings on MCrAlY-type bondcoats associated with the formation of the thermally grown oxide, J. Mater. Sci. 44 (2009).

[60] M. Seraffon, Performances of Air Plasma Sprayed Thermal Barrier Coatings for Industrial Gas Turbines, 2012.